

**Absorption and gain saturable nonlinearities in erbium-doped optical microcavities**Yong Hu,<sup>1</sup> Yan Bai,<sup>1</sup> Yang Liu,<sup>1</sup> Shulin Ding,<sup>1</sup> Shiyue Hua,<sup>1</sup> Xiaoshun Jiang<sup>1,\*</sup> and Min Xiao<sup>1,2</sup><sup>1</sup>*National Laboratory of Solid State Microstructures, College of Engineering and Applied Sciences, and School of Physics, Nanjing University, Nanjing 210093, China*<sup>2</sup>*Department of Physics, University of Arkansas, Fayetteville, Arkansas 72701, USA*

(Received 23 May 2019; published 24 September 2019)

Nonlinear non-Hermitian systems with saturable nonlinearities give rise to versatile phenomena that have no counterparts in linear systems. Here, we theoretically and experimentally demonstrate saturable nonlinearity (saturable absorption and gain) of erbium ions doped in silica microcavities at different concentrations. Our results show that when the doped concentration is low, the single isolated model agrees well with the experimental results, and also can be used as a basic description of highly doped samples to analyze the saturable nonlinearity. Yet, for highly doped microcavities we find that the clustering effect shall be also taken into account in order to match experimental data and to achieve a reasonable agreement. To confirm our finding, we experimentally characterize the saturable nonlinearity for ion concentrations varying from 1.0 to  $5.0 \times 10^{19} \text{ cm}^{-3}$ . Our experiment shows excellent consistency with the theory, which in turn suggests other potential applications of the theory based on saturable nonlinearity, including optical bistability and nonlinear parity-time symmetry.

DOI: [10.1103/PhysRevA.100.033831](https://doi.org/10.1103/PhysRevA.100.033831)**I. INTRODUCTION**

Optical saturable nonlinearity as a nonlinear function of light intensity has been studied since the 1960s [1–3], and a variety of applications have been discovered since then. Among these applications include, but are not limited to, optical bistable devices [4–6], mode locking lasers [7–12], and ultrafast all-optical switches based on intersubband transitions [13,14]. Owing to the excellent confinements and large built-up factors [15], whispering-gallery mode (WGM) microcavities can easily establish optical saturation and thus become an excellent platform to investigate intensity-dependent saturable nonlinearities.

Recently, concepts drawn from non-Hermitian physics and parity-time (PT) symmetry have attracted considerable attention [16–19]. As a counterpart to loss, gain is very important in the construction of a PT-symmetric system [20–29]. In previous treatments, optical gain was mainly considered in a linear fashion [21–24], i.e., it was assumed to be independent of the field intensity. This drawback motivates us to carry out a systematic investigation of the problem, in particular, when optical saturable nonlinearity is non-negligible. We notice that in recent years, the research on gain saturation has led to many interesting phenomena such as nonreciprocal propagation [30–33], robust wireless power transfer [34], and adiabatic state switching after proper encircling exceptional points [35]. Of importance, the interplay between saturable gain and loss gives rise to effects [36–39] which include the order reversing of PT phase transitions [36] and the locking of light propagation directions [39].

Despite these impressive achievements, the underlying physics of the mechanism of saturable gain and loss is lack of a clear interpretation and modeling. Here, we theoretically and experimentally study the saturable nonlinearity in erbium-ion-doped optical microcavities with different doping concentrations. In previous work, erbium-doped and other rare-earth-doped WGM microcavities with different kinds of structures have been studied for the realization of ultra-low-threshold microlasers [40–50]. Recently, the gain transmission spectra in the rare-earth-doped microcavities have been investigated with a certain doping concentration [51–56]. For example, Refs. [51,53] observed spectral evolutions from Lorentzian dips to Fano-like resonances and then to Lorentzian peaks. As a result, a detailed analysis at high signal power levels remains unavailable, especially when the pump field is terminated. Here, we theoretically and experimentally investigated the saturable absorption and gain nonlinearities in erbium-ion-doped microcavities with different doping concentrations. By comparing experiment with theory, we find that the isolated ion model [57] gives a great description for low doping concentrations, but for high doping concentrations, a compound model of isolated and clustered ions [58,59] has to be adopted to give a satisfactory description. To support our conclusion, we fabricated erbium-ion-doped silica microtoroid cavities with doping concentrations changing from 1.0 to  $5.0 \times 10^{19} \text{ cm}^{-3}$ . Our results clearly indicate that both the coefficients of saturable absorption and gain increase along with the growth of ion concentration, while their increment deviates from linearity in the heavily doped region because of the clustering effect.

We organize our article as follows. In Sec. II, we first present a theoretical analysis of the saturable nonlinearity of erbium-doped microcavities. In Sec. III, we then experimentally investigate the saturable nonlinearity of the

\*Corresponding author: [jxs@nju.edu.cn](mailto:jxs@nju.edu.cn)

erbium-doped microtoroid cavities by varying the signal and pump power for different doping concentrations. By fitting the experimental data with the models, we obtain nonlinearity coefficients and saturable intensities which agree well with our theoretical predictions.

## II. THEORETICAL MODEL

The theoretical analyses are based on the coupled mode theory (CMT) [60,61] of a microresonator coupled with a waveguide and the rate equations [57] of a three-level ion system that includes the clustering effect. In the experiment, we consider a signal mode at 1550-nm wavelength and a 1480-nm pump mode which respectively correspond to the transition band between the excited ( $^4I_{13/2}$  denoted by  $|e\rangle$ ) and the ground ( $^4I_{15/2}$  denoted by  $|g\rangle$ ) states of erbium, and the transition between the metastable ( $^4I_{11/2}$  denoted by  $|m\rangle$ ) and the ground states [see Fig. 1(b)]. The experimental setup for the saturable nonlinearity measurement is schematically shown in Fig. 1(a). Experimentally, both the signal and the pump are launched into the microtoroid cavity from port 1 and then coupled to the microcavity with a tapered fiber [51]. The output transmissions are extracted from the same tapered fiber and detected at port 2. The polarizations of the pump and signal lasers are adjusted by FPC1 and FPC2, respectively, to match the whispering-gallery modes supported by the microtoroid cavity.

### A. Isolated single-ion model

At low erbium concentrations, the distance between each ion is large. Therefore, in such a case all ions are assumed to be isolated, and we employ the isolated ion model to describe the saturable nonlinearity in the microcavities. In this physical picture, the coupled equations for the pump and signal modes and the rate equations [51,57] of the simplified three-level structure can be written as follows:

$$\frac{da_s}{dt} = [i\Delta_s + g_s - (\gamma_s^0 + \kappa_s)/2]a_s + \sqrt{\kappa_s} s_{in}^s, \quad (1)$$

$$\frac{da_p}{dt} = [i\Delta_p + g_p - (\gamma_p^0 + \kappa_p)/2]a_p + \sqrt{\kappa_p} s_{in}^p, \quad (2)$$

$$g_s = \frac{Nc}{2n_s} \frac{\sigma_p^a \sigma_s^e \tau_{21} \Phi_p - \sigma_p^e \sigma_s^a \tau_{32} \Phi_p - \sigma_s^a}{(\sigma_s^a + \sigma_s^e) \tau_{21} \Phi_s + (\sigma_p^e \tau_{21} + \sigma_p^a \tau_{32} + \sigma_p^e \tau_{32}) \Phi_p + (\sigma_p^e \sigma_s^e + \sigma_p^a \sigma_s^e + \sigma_p^e \sigma_s^a) \tau_{21} \tau_{32} \Phi_s \Phi_p + 1}, \quad (7)$$

$$g_p = \frac{Nc}{2n_p} \frac{-\sigma_s^e \tau_{21} \Phi_s - \sigma_p^a}{(\sigma_s^a + \sigma_s^e) \tau_{21} \Phi_s + (\sigma_p^e \tau_{21} + \sigma_p^a \tau_{32} + \sigma_p^e \tau_{32}) \Phi_p + (\sigma_p^e \sigma_s^e + \sigma_p^a \sigma_s^e + \sigma_p^e \sigma_s^a) \tau_{21} \tau_{32} \Phi_s \Phi_p + 1}. \quad (8)$$

With these results, we are now ready to look at the behavior of the signal mode in two major cases: saturable absorption (without pump) and gain (with pump). The saturable absorption and gain are primarily due to band filling so as to reach the steady state [3]. That is, when the signal power increases, photon absorption and emission intend to fill the excited state, which in turn blocks further absorption and emission. Because it is not straightforward to examine saturable phenomena directly using Eqs. (7) and (8), instead we will make some simplifications and approximations as demonstrated below.

$$\frac{dN_3}{dt} = -\frac{N_3}{\tau_{32}} + (N_1 \sigma_p^a - N_3 \sigma_p^e) \Phi_p, \quad (3)$$

$$\frac{dN_2}{dt} = -\frac{N_2}{\tau_{21}} + \frac{N_3}{\tau_{32}} + (N_1 \sigma_s^a - N_2 \sigma_s^e) \Phi_s. \quad (4)$$

Here,  $\Phi_{s,p} = c\Gamma_{s,p}|a_{s,p}|^2/V_{(s,p)m}h\nu_{s,p}n_{s,p}$ , where  $a_{s,p}$  represents the signal or pump field amplitude inside the microcavity ( $|a_{s,p}|^2$  are their corresponding energies within the cavity),  $\Delta_{s,p} = \omega_{s0,p0} - \omega_{s,p}$  are, respectively, the frequency detunings between the cavity modes at the signal and pump modes ( $\omega_{s0,p0}$ ) and their input laser frequencies  $\omega_{s,p}$ ,  $\gamma_{s,p}^0$  are the intrinsic decay rates of the cavity modes without the effect of the erbium ions,  $\kappa_{s,p}$  are the coupling coefficients between the cavity and the coupled waveguide for signal and pump,  $s_{in}^{s,p}$  stands for signal or pump input field through the tapered fiber from port 1,  $\sigma_{s,p}^a$  and  $\sigma_{s,p}^e$  are, respectively, the absorption and emission cross sections,  $V_{(s,p)m}$  are the mode volumes,  $n_{s,p}$  are the refractive indices,  $N_{1,2,3}$  are, respectively, the ion populations in the ground, excited, and metastable states with the total effective doped ion number  $N = N_1 + N_2 + N_3$ , and  $\Gamma_{s,p}$  are the overlap factors between the optical fields and the doped ion region. We set  $\Gamma_{s,p} = 1$  for uniformly distributed ions in sol-gel silica films on silicon. Note that for all the above variables, the subscripts or superscripts  $s$  and  $p$  represent the signal and pump modes, respectively. On the other hand, according to previous results [51,57], the intracavity gain coefficients  $g_{s,p}$  for the signal and pump fields in Eqs. (1) and (2) take the form of

$$g_s = \frac{c}{2n_s} (-N_1 \sigma_s^a + N_2 \sigma_s^e), \quad (5)$$

$$g_p = \frac{c}{2n_p} (-N_1 \sigma_p^a + N_3 \sigma_p^e). \quad (6)$$

To study the saturable nonlinearity, we focused on the situation when the system reaches its equilibrium. As such, by setting the time derivatives in Eqs. (3) and (4) to be zero, we have the steady-state equations of ion populations of the states. After some algebra, the signal and pump gains in Eqs. (5) and (6) can be reexpressed as

### 1. Saturable absorption nonlinearity

First of all, let us look at the case of saturable absorption nonlinearity. Without the input pump power, the signal ‘‘gain’’ (i.e., loss) can be simplified by setting  $\Phi_p = 0$  in Eq. (7), which yields

$$g_s = -\frac{Nc}{2n_s} \frac{\sigma_s^a}{(\sigma_s^a + \sigma_s^e) \tau_{21} \Phi_s + 1}. \quad (9)$$

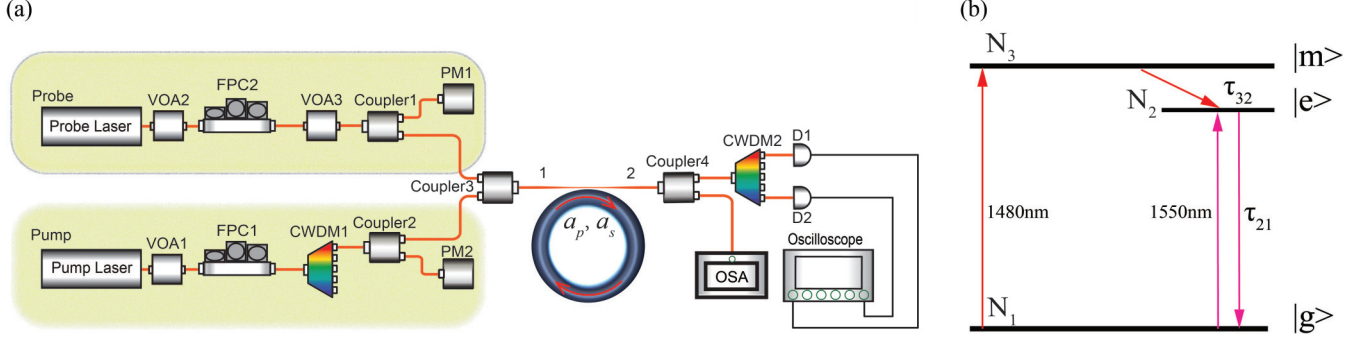


FIG. 1. (a) Schematic of the experimental setup where the pump light is only on in the measurements of gain saturable nonlinearity. VOA, PM, FPC, CWDM, respectively, denote variable optical attenuator, power meter, fiber polarization controller, and coarse wavelength division multiplexer. (b) The three-level erbium ion energy diagram.

Note that in this case, the system actually experiences loss, and the saturable absorption has the form

$$\gamma_{Er} = 2|g_s| = \frac{f_0}{1 + (\sigma_s^a + \sigma_s^e)\tau_{21}\Phi_s} = \frac{f_0}{1 + E_s/E_{sat}}, \quad (10)$$

where  $f_0$  is the coefficient of the saturable absorption and  $E_{sat}$  is the saturated energy. From Eqs. (9) and (10), the saturable absorption nonlinearity is mainly determined by two major parameters:

$$f_0 = Nc\sigma_s^a/n_s, \quad (11)$$

$$E_{sat} = \frac{V_s h\nu_s n_s}{(\sigma_s^a + \sigma_s^e)\tau_{21}c\Gamma_s}. \quad (12)$$

Physically, Eq. (10) implies that the cavity decay rate  $\gamma_{Er}$  induced by doped ion absorption will become saturated along with the increment of the signal power. These have been confirmed in our theoretical simulations as shown in Fig. 2(a). In contrast, Fig. 2(b) presents the numerical results based on the compound model (which shall be discussed shortly). The comparison between Figs. 2(a) and 2(b) indicates that at low doping concentration, the features of saturable absorption are

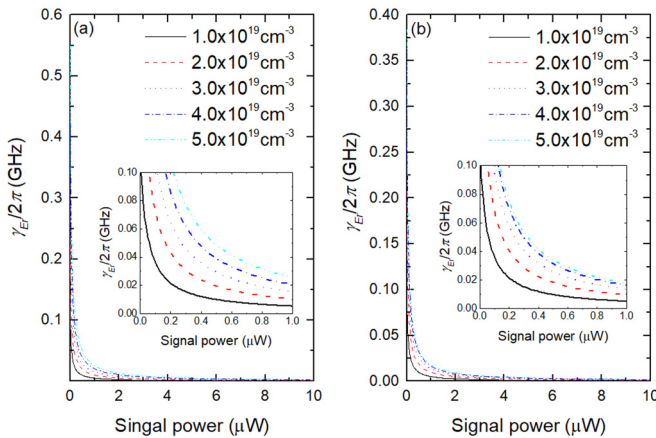


FIG. 2. Cavity decay rate induced by the doped ions vs signal power for different concentrations. (a) Isolated single-ion model. (b) Compound model where the ratios of single to clustered ions are adopted from Table I. Insets zoom in on the decay rates for the low power inputs.

mostly characterized by the isolated single-ion model. From Eqs. (11) and (12), the coefficient of the saturable absorption nonlinearity is directly proportional to the doping population concentration. This has also been verified in our experiment [see black squares and line in Fig. 6(b)].

## 2. Saturable gain nonlinearity

When the input pump power becomes strong and crucial, the signal inside the microcavity will experience saturable gain nonlinearity. To analyze this case, we first consider the gain saturation for a fixed pump power but by varying the signal power, and then for a fixed signal but by changing the pump power.

For the fixed pump power, the signal gain follows a similar saturable form as Eq. (10):

$$g_{Er} = \frac{g_0}{1 + E_s/E_{sat}^s}, \quad (13)$$

where

$$g_0 = Nc/2n_s(\sigma_p^a\sigma_s^e\tau_{21}\Phi_p - \sigma_p^e\sigma_s^a\tau_{32}\Phi_p - \sigma_s^a), \quad (14)$$

$$E_{sat}^s = \frac{1 + (\sigma_p^e\tau_{21} + \sigma_p^a\tau_{32} + \sigma_p^e\tau_{32})\Phi_p}{(\sigma_s^a + \sigma_s^e) + (\sigma_p^e\sigma_s^e + \sigma_p^a\sigma_s^e + \sigma_p^e\sigma_s^a)\tau_{32}\Phi_p} \times \frac{V_s h\nu_s n_s}{(\sigma_s^a + \sigma_s^e)\tau_{21}c\Gamma_s}. \quad (15)$$

Equation (13) shows that the signal gain will approach its limit as increasing the power. This behavior is shown in Fig. 3 by numerical simulations.

For a fixed signal power, the signal gain saturation induced by the variation of the pump power is still described with Eq. (7), which cannot be easily transformed to a simple form. To reveal its nature of nonlinearity, we numerically compute this gain saturation as a function of the dropped pump power within the microcavity. The result is given in Fig. 4(a), which clearly exhibits the saturable feature.

## B. Compound model of single and clustered ions

Increasing the erbium ion concentration results in a decreasing distance between neighboring ions, which in turn enables rapid energy transfer from excited ions to

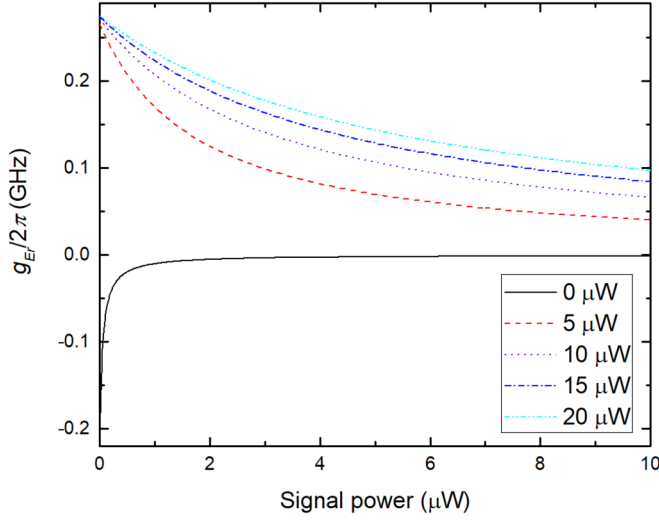


FIG. 3. Signal gain vs input signal power for different pump powers. The doping concentration was  $2.0 \times 10^{19} \text{ cm}^{-3}$ .

neighbors [62,63]. This energy transfer thus initiates the clustering effect [58,59,64,65], in which the excited ion transfers its energy to another one and excites it to higher energy states, while itself decaying nonradiatively to the ground state. Owing to the instability or metastability of the higher energy states, ions in these states will decay rapidly back to the excited state nonradiatively and meanwhile transfer the energy to nearby excited ions. In this way, the process repeats itself. As a result, when the ions of one cluster are excited, only one ion can remain excited and emit signal photons while all the others rapidly relax to the ground state nonradiatively [64]. Alternatively, the clustering effect greatly reduces the effective ion concentration.

To catch the essential physics, for simplicity we theoretically divide the doped ions into two different groups: single

isolated ones and clusters with corresponding numbers  $N_S$  and  $N_C^m$  (here  $m$  means  $m \geq 2$  ions in a cluster). Similar to the paired-ion model [62,63], we utilize the two-level model to describe the clustered ions. With these considerations, the rate equations now can be written as follows:

$$\frac{dN_{3S}}{dt} = -\frac{N_{3S}}{\tau_{32}} + (N_{1S}\sigma_p^a - N_{3S}\sigma_p^e)\Phi_p, \quad (16)$$

$$\frac{dN_{2S}}{dt} = -\frac{N_{2S}}{\tau_{21}} + \frac{N_{3S}}{\tau_{32}} + (N_{1S}\sigma_s^a - N_{2S}\sigma_s^e)\Phi_s, \quad (17)$$

$$\begin{aligned} \frac{dN_{2C}^m}{dt} = & -\frac{mN_{2C}^m}{\tau_{21}} + (mN_{1C}^m\sigma_p^a - mN_{2C}^m\sigma_p^e)\Phi_p \\ & + (mN_{1C}^m\sigma_s^a - mN_{2C}^m\sigma_s^e)\Phi_s, \end{aligned} \quad (18)$$

where  $N_S = N_{1S} + N_{2S} + N_{3S}$ ,  $N_C^m = N_{1C}^m + N_{2C}^m$ ,  $N_C = \sum_2^\infty mN_C^m$ , and the total population density  $N = N_S + N_C$ . The factor  $m$  in front of every population density in Eq. (18) indicates  $m$  possibilities for the excited ions to decay to the ground state and vice versa. Similar to Eq. (5), the signal gains resulting from the isolated single ions and clustered can be represented by

$$g_{SS} = \frac{c}{2n_s}(-N_{1S}\sigma_s^a + N_{2S}\sigma_s^e), \quad (19)$$

$$g_{SC}^m = \frac{c}{2n_s}\{-[mN_{1C}^m + (m-1)N_{2C}^m]\sigma_s^a + N_{2C}^m\sigma_s^e\}. \quad (20)$$

In Eq. (20), the factor  $mN_{1C}^m + (m-1)N_{2C}^m$  means the population in the ground state, which contains the  $mN_{1C}^m$  population in the ground state throughout the processes and the  $(m-1)N_{2C}^m$  population generated after the rapid multiple-energy-transfer processes. After these processes, every cluster is left with only one excited ion. Thus the population in the excited state is  $N_{2C}^m$ .

With the use of Eqs. (16)–(20), the signal gains induced by different components can be evaluated as

$$g_{SS} = \frac{N_S c}{2n_s} \frac{\sigma_p^a \sigma_s^e \tau_{21} \Phi_p - \sigma_p^e \sigma_s^a \tau_{32} \Phi_p - \sigma_s^a}{(\sigma_s^a + \sigma_s^e) \tau_{21} \Phi_s + (\sigma_p^e \tau_{21} + \sigma_p^a \tau_{32} + \sigma_p^e \tau_{32}) \Phi_p + (\sigma_p^e \sigma_s^e + \sigma_p^a \sigma_s^e + \sigma_p^e \sigma_s^a) \tau_{21} \tau_{32} \Phi_s \Phi_p + 1}, \quad (21)$$

$$g_{SC}^m = \frac{N_C^m c - (m-1) \tau_{21} \sigma_s^a (\sigma_s^a + \sigma_s^e) \Phi_s - m \tau_{21} \sigma_s^a (\sigma_p^a + \sigma_p^e) \Phi_p + \tau_{21} (\sigma_s^a + \sigma_s^e) \sigma_p^a \Phi_p - m \sigma_s^a}{2n_s (\sigma_s^a + \sigma_s^e) \tau_{21} \Phi_s + (\sigma_p^a + \sigma_p^e) \tau_{21} \Phi_p + 1}. \quad (22)$$

Hence, the total gain experienced by the signal light is

$$g_s = g_{SS} + \sum_2^\infty g_{SC}^m. \quad (23)$$

From numerical simulations, we find that in the presence of ion clusters, the features of saturable absorption and gain are still clear, as shown in Figs. 2(b) and 4(b). Meanwhile, the coefficient of the saturable nonlinearity is reduced (compared with the isolated model) due to the reduced concentration of effectively doped ions. This change has been captured in Fig. 6(b) (red triangles). The account of clustered ions reduces to the paired ions for  $m = 2$  and returns to the two-level single-isolated-ion model when  $m = 1$ . To have a better

understanding of the model, Table I lists the estimated ratios of different ion compositions by assuming the mixtures of single ions and clusters having two or three ions.

### III. EXPERIMENTAL TEST

To verify our theory with the experiment, we have examined the saturable nonlinearity for various erbium ion concentrations over the range of  $1.0\text{--}5.0 \times 10^{19} \text{ cm}^{-3}$ . The fabrication procedure of the sol-gel films was the same as that used in Refs. [41,49]. In the experiment, we recorded the transmission spectra of the output signal through the tapered-fiber-coupled microcavity system [which is depicted

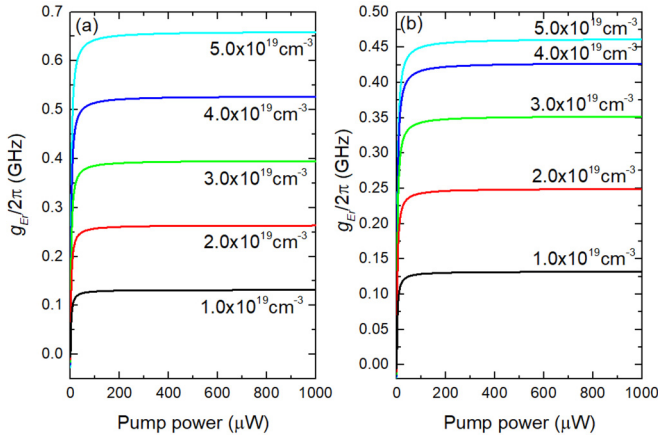


FIG. 4. Signal gain vs input pump power at different doping concentrations by fixing the signal input power. (a) Single-ion model. (b) Compound model. The ratios of the clustering ions used in the calculations are listed in Table I.

in Fig. 1(a)]. During the measurement, the coupling coefficient was kept unchanged. For the erbium-doped microtoroid cavity here, the decay rate for the signal mode is

$$\gamma_s = \gamma_s^{\text{intrinsic}} + \gamma_s^{\text{ext}} = \gamma_s^0 + \gamma_s^{\text{Er}} + \gamma_s^{\text{ext}}, \quad (24)$$

where  $\gamma_s^{\text{intrinsic}}$ ,  $\gamma_s^0$ ,  $\gamma_s^{\text{Er}}$ , and  $\gamma_s^{\text{ext}}$  are, respectively, the intrinsic decay rate, the intrinsic decay rate without the doped ions, the decay rate induced by ion absorption, and the extra decay rate with the coupling of the waveguide. The intrinsic cavity decay rate takes the form of

$$\gamma_s^{\text{intrinsic}} = \gamma_s^0 + \gamma_s^{\text{Er}} = \gamma_s^0 + 2g_s = \gamma_s^0 + f_0/(1 + E_s/E_{\text{sat}}), \quad (25)$$

which can be experimentally obtained by fitting the transmission spectrum with the CMT. In other words, we used Eq. (25) to fit our experimental data.

### A. Saturable absorption

In the experiment, we first study the saturable absorption case without the pump input. By gradually increasing the input signal power, a series of narrow Lorentzian transmission spectra were obtained with an oscilloscope after a photodetector [see Fig. 1(a)]. The intrinsic cavity decay rate  $\gamma_s^{\text{intrinsic}}$  [see Eq. (25)] was retrieved by fitting the spectra with the CMT. Figure 5(a) shows the experimentally extracted intrinsic cavity decay rate versus the signal power for an ion concentration of

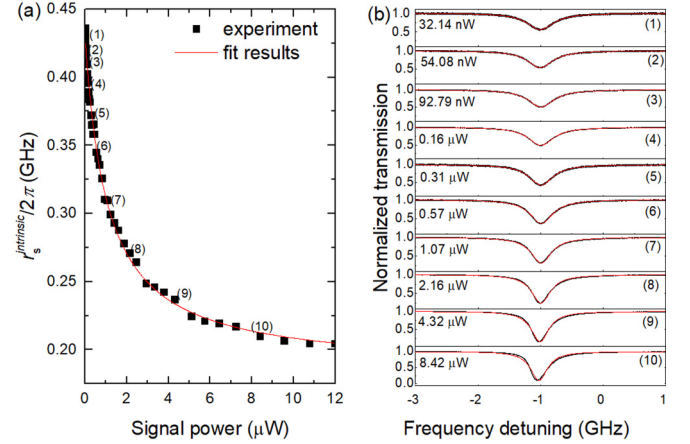


FIG. 5. (a) Total intrinsic cavity decay rate for the signal mode vs input signal power. The concentration was  $2.0 \times 10^{19} \text{ cm}^{-3}$ . (b) Without pump input, typical transmission spectra obtained by increasing signal power. Spectra (1)–(10) refer to squares marked in (a).

$2.0 \times 10^{19} \text{ cm}^{-3}$ . As expected, the intrinsic cavity decay rate decreases with the increased signal power and then gradually approaches the limit  $\gamma_s^0$  in the high-power regime. Typical transmission spectra are shown in Fig. 5(b) for different signal powers. As we can see, as the signal power increases, the linewidth and depth of the characteristic transmission dip becomes narrower and deeper and changes from the under-coupling regime to the nearly critical-coupling regime. The last transmission spectrum labeled as (10) in Fig. 5(b) looks rather asymmetric because of the thermal-optical effect [66]. To avoid this unwanted effect, in the experiment we stopped measurements upon the occurrence of such asymmetric spectra.

To systematically investigate this nonlinearity, we carefully examined saturable absorption as a function of the signal power at different ion concentrations of  $1.0 \times 10^{19} \text{ cm}^{-3}$ ,  $3.0 \times 10^{19} \text{ cm}^{-3}$ ,  $4.0 \times 10^{19} \text{ cm}^{-3}$ , and  $5.0 \times 10^{19} \text{ cm}^{-3}$ , respectively. The experimental results are plotted in Fig. 6(a). As one can see, at a higher concentration, because the loss caused by the doped erbium ions becomes large, the saturable nonlinearity accordingly becomes more significant. To avoid the linewidth broadening induced by the thermal effect [66], different maximal signal powers were chosen in response to different intrinsic cavity decay rates. Figure 6(b) compares the experimentally obtained  $f_0$  (saturable absorption nonlinearity coefficient) with the numerically computed  $f_0$  based on both

TABLE I. Ratios of single ions and clustered ions of compound model calculations.

Concentration	Ratio (%)	Single ions ( $m = 1$ )	Paired ions ( $m = 2$ )	Clusters ( $m = 3$ )	Effective concentration
$1.0 \times 10^{19} \text{ cm}^{-3}$		100	0	0	$1.0 \times 10^{19} \text{ cm}^{-3}$
$2.0 \times 10^{19} \text{ cm}^{-3}$		90	3.5	1	$1.89 \times 10^{19} \text{ cm}^{-3}$
$3.0 \times 10^{19} \text{ cm}^{-3}$		80	7	2	$2.67 \times 10^{19} \text{ cm}^{-3}$
$4.0 \times 10^{19} \text{ cm}^{-3}$		65	13	3	$3.24 \times 10^{19} \text{ cm}^{-3}$
$5.0 \times 10^{19} \text{ cm}^{-3}$		50	10	10	$3.50 \times 10^{19} \text{ cm}^{-3}$

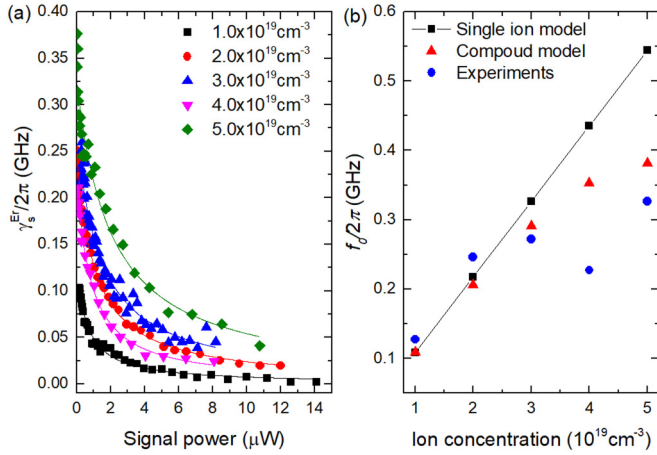


FIG. 6. (a) Cavity decay rate induced by erbium absorption vs input signal power for different ion concentrations. The symbols are experimental results and the solid lines are theoretical curves with the form of  $\gamma_s^{\text{Er}}$  in Eq. (25). (b) At different ion concentrations, saturable nonlinearity coefficients with the single-ion model (black squares and solid line) and the compound model (red triangles) compared with experimental results (blue circles). Here parameters are  $\sigma_s^a = 6.67 \times 10^{-21} \text{ cm}^2$ ,  $\sigma_s^e = 7.0 \times 10^{-21} \text{ cm}^2$ ,  $\sigma_p^a = 6.0 \times 10^{-21} \text{ cm}^2$ ,  $\sigma_p^e = 5.5 \times 10^{-21} \text{ cm}^2$ ,  $\tau_{21} = 6 \text{ ms}$ ,  $\tau_{32} = 10 \mu\text{s}$ ,  $n_s = n_p = 1.45$ ,  $V_{(s,p)m} = 740 \mu\text{m}^3$ . Again, the ratios of the clustering ions used in the theoretical calculations are listed in Table I.

the single-ion model and the compound model at different ion concentrations. In the theoretical calculations, we used the ratios of the single and clustering ions summarized in Table I, as they were in a reasonable range as suggested by Ref. [58]. From Fig. 6(b), one can deduce that when the ion concentration is small, the experimental results follow the single-ion model. However, as the concentration increases, the experimental data start to deviate from that simple model. Alternatively, the paired ions and clustering effects were taken into account. For the sake of simplicity, we used the same parameters as those for single ions to analyze the saturable nonlinearity with the compound model of single and clustered ions. The results given by the compound model agree well with the experimental measurements, in both the low- and high-concentration regimes.

### B. Saturable gain

With the pump on, the erbium-doped sol-gel silica microcavity becomes an active system with stimulated emission to balance a portion of the system loss. When the pump power surpasses a certain threshold, the system acts as a laser, as fully reported previously [41–50]. To study the saturable gain nonlinearity, we restrict the pump power below the lasing threshold. Also, we analyzed the saturable gain nonlinearity by fixing either the pump power or the input signal power.

For a given pump power, the gain saturable nonlinearity was experimentally demonstrated via measuring the transmission spectra of the signal mode by increasing the input signal power at an ion concentration of  $2.0 \times 10^{19} \text{ cm}^{-3}$  (see Fig. 7). The experimentally extracted signal gain is consistent with our theoretical curve using Eq. (13), see Fig. 7(a).

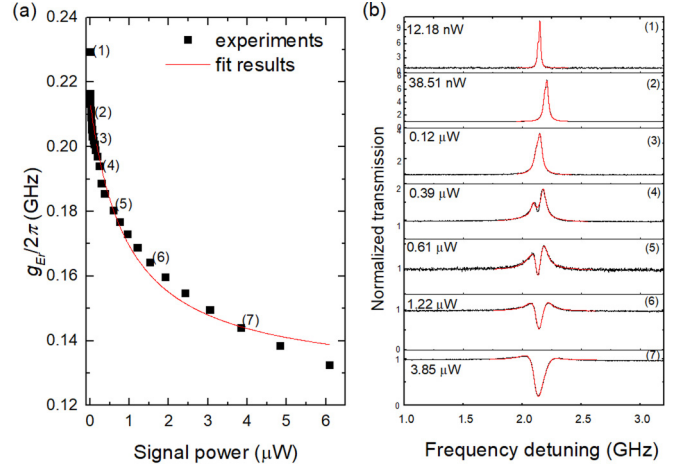


FIG. 7. Characterization of the saturable gain nonlinearity at a fixed pump power ( $300 \mu\text{W}$ ). (a) Signal gain as a function of signal power at an ion concentration of  $2.0 \times 10^{19} \text{ cm}^{-3}$ . (b) Typical transmission spectra by increasing signal power. Spectra (1)–(7) refer to squares marked in (a).

As shown in Fig. 7(b), by reducing the signal power, the spectral profiles transform from Lorentzian dips to the Fano line shapes and finally flip to peaks. Similar to the saturable absorption, the intrinsic cavity decay rate decreases with increasing the signal power and eventually reaches a constant limit. Considering the similarity between Eqs. (11) and (14), we expect similar observations for other ion concentrations.

At a fixed signal power, the signal gain saturation was probed through measuring the signal transmission spectra by changing the dropped pump power instead for the doping concentration of  $2.0 \times 10^{19} \text{ cm}^{-3}$ . The measurements are illustrated in Fig. 8. Specifically, Fig. 8(a) presents the measured signal gain versus the theoretical prediction by Eq. (13) in terms of the dropped pump powers. Figure 8(b) accordingly displays the typical signal transmission spectra for various pump powers. As the pump power increases, the observed

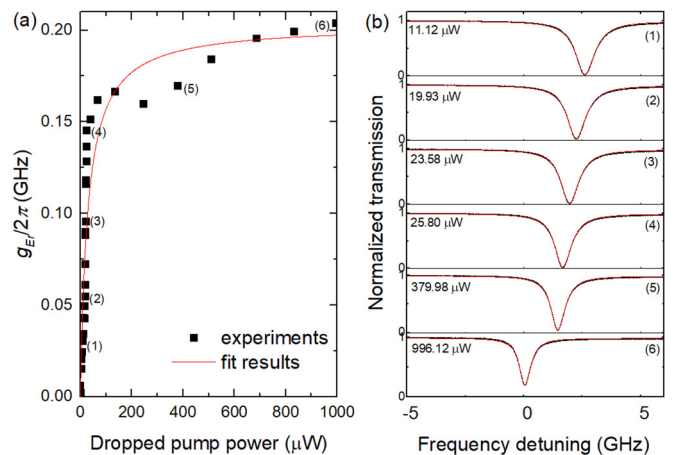


FIG. 8. For a fixed signal power of  $0.14 \mu\text{W}$ , (a) signal gain vs dropped pump power at a concentration of  $2.0 \times 10^{19} \text{ cm}^{-3}$ , and (b) typical transmission spectra by increasing dropped pump power. Spectra (1)–(6) in (b) correspond to squares labeled in (a).

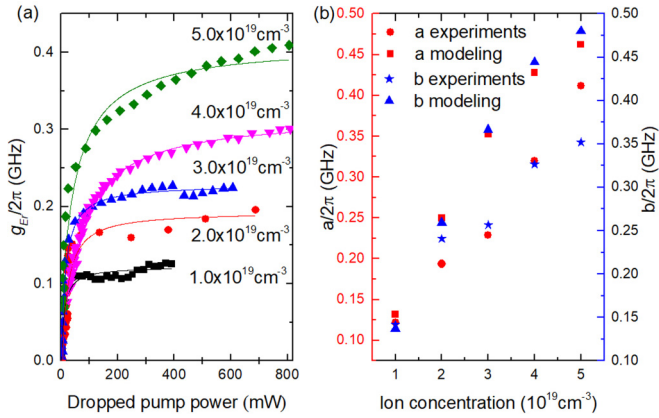


FIG. 9. Characterization of the gain saturable nonlinearity at a fixed signal power of  $0.14 \mu\text{W}$ . (a) Signal gain vs dropped pump power for five different concentrations. (b) Experimentally measured parameters  $a$  and  $b$  compared with theoretically computed results based on the compound model.

spectral linewidth narrowing is a result of the increased gain. A redshift was also observable for the shifted resonance locations because of the thermal effect [66]. In the experiment, we have seen that the spectral profiles changed from Lorentzian dips to asymmetric Fano line shapes and then to peaks at other higher- $Q$  modes (not shown). Instead, low  $Q$ -factor modes were used to avoid the Fano lines and peaks to simplify the data analysis.

As discussed in Sec. II B, when the doping concentration is increased, the paired ions as well as the clustering effect become important in the analysis and the compound model shall be considered. To check this, we have further examined the saturable gain nonlinearity at other concentrations ( $1.0, 3.0, 4.0,$  and  $5.0 \times 10^{19} \text{ cm}^{-3}$ ), and the experimental data are given in Fig. 9. Figure 9(a) shows the comparison of the measured signal gain with the computed gain as a function of the dropped pump power. As one can see, the experimental data are well fit with the gain saturable forms, which is a saturable function of the energy for the pump light,  $a - b/(1 + E_p/E_{\text{sat}}^p)$ . Here, the parameters  $a$  and  $b$  are determined by the doped ion concentration, and this has been confirmed in Fig. 9(b). As revealed in Fig. 9(b), by enlarging the ion concentration, these two parameters exhibit the same trend as that reflected by the numerical calculations. Note that the values of  $a$  and  $b$  are comparable to the saturable absorption nonlinearity coefficient  $f_0$  [see Fig. 6(b)]. This in turn implies that both the saturable absorption and gain are primarily due to band filling to reach the steady state [3].

The observed nonmonotonic behavior in Figs. 8(a) and 9(b) might be attributed to the unstable coupling between the fiber taper and the optical microcavity during the measurement, which correspondingly makes the dropped optical power unstable in the optical microcavity. In the experiment, the dropped pump power is adjusted by controlling the pump frequency detuning with respect to the cavity resonance frequency. For higher pump power, the pump frequency is closer to the resonance frequency of the cavity mode, which leads to the dropped pump power being more sensitive to variation of the coupling distance. So the nonmonotonic behavior becomes obvious for higher pump power. Also, since the intrinsic optical  $Q$  factors in highly doped microcavities are lower than the lower doped ones, the total optical  $Q$  factors are insensitive to the variation of coupling between the fiber taper and the optical microcavity. As a result, the nonmonotonic behavior disappears for higher concentrations.

#### IV. CONCLUSIONS

In summary, we have theoretically and experimentally studied saturable nonlinearity (absorption and gain) in optical microcavities doped with erbium ions. Our results suggest that at low ion concentrations, the isolated single-ion model gives a good account of the phenomena. For heavily doped cases, however, the more practical compound model that combines single and clustered ions shows a better agreement with experiment. Alternatively, the observed deviation from the isolated single-ion model at high concentrations is mainly caused by clustered ion quenching. To improve the coefficients of the saturable nonlinearity, other codoping methods could be used [67–70] to suppress the clustering effect.

Although our detailed analysis on the saturable nonlinearity was made with erbium-doped silica microcavities, it can be easily extended to other rare-earth-doped systems. With these results, we also expect to observe optical bistability induced by the saturable nonlinearity, in single or coupled PT-symmetric microcavities [32,35,71]. Nonlinear PT-symmetric microcavities with both intensity-dependent gain and loss are another interesting subject for further exploration [36–39].

#### ACKNOWLEDGMENTS

This research was supported by the National Key R&D Program of China (Grants No. 2016YFA0302500 and No. 2017YFA0303703), the National Natural Science Foundation of China (NSFC) (Grants No. 61922040, No. 11574144, No. 61435007, and No. 11621091), and the Fundamental Research Funds for the Central Universities (Grant No. 021314380149).

- [1] W. W. Rigrod, *J. Appl. Phys.* **34**, 2602 (1963).
- [2] M. Hercher, *Appl. Opt.* **6**, 947 (1967).
- [3] R. N. Zitter, *Appl. Phys. Lett.* **14**, 73 (1969).
- [4] A. Szöke, V. Daneu, J. Goldhar, and N. A. Kurnit, *Appl. Phys. Lett.* **15**, 376 (1969).
- [5] E. Garmire, *IEEE J. Quantum Electron.* **25**, 289 (1989).
- [6] L. Xu, B. C. Wang, V. Baby, I. Glesk, and P. R. Prucnal, *IEEE Photonic Technol. Lett.* **14**, 149 (2002).
- [7] H. A. Haus, *IEEE J. Quantum Electron.* **11**, 736 (1975).
- [8] H. A. Haus, *J. Appl. Phys.* **46**, 3049 (1975).
- [9] R. Fluck, B. Braun, E. Gini, H. Melchior, and U. Keller, *Opt. Lett.* **22**, 991 (1997).
- [10] L. Orsila, L. A. Gomes, N. Xiang, T. Jouhti, and O. G. Okhotnikov, *Appl. Opt.* **43**, 1902 (2004).
- [11] S. Kivistö, R. Koskinen, J. Paajaste, S. D. Jackson, M. Guina, and O. G. Okhotnikov, *Opt. Express* **16**, 22058 (2008).
- [12] Q. Bao, H. Zhang, Y. Wang, Z. Ni, Y. Yan, Z. X. Shen, K. P. Loh, and D. Y. Tang, *Adv. Funct. Mater.* **19**, 3077 (2009).

- [13] Y. Li, A. Bhattacharyya, C. Thomidis, T. D. Moustakas, and R. Paiella, *Opt. Express* **15**, 17922 (2007).
- [14] N. Iizuka, K. Kaneko, and N. Suzuki, *IEEE J. Quantum Electron.* **42**, 765 (2006).
- [15] K. J. Vahala, *Nature (London)* **424**, 839 (2003).
- [16] L. Feng, R. El-Ganainy, and L. Ge, *Nat. Photon.* **11**, 752 (2017).
- [17] R. El-Ganainy, K. G. Makris, M. Khajavikhan, Z. H. Musslimani, S. Rotter, and D. N. Christodoulides, *Nat. Phys.* **14**, 11 (2018).
- [18] J. Wen, X. Jiang, L. Jiang, and M. Xiao, *J. Phys. B: At. Mol. Opt. Phys.* **51**, 222001 (2018).
- [19] S. K. Ozdemir, S. Rotter, F. Nori, and L. Yang, *Nat. Mater.* **18**, 783 (2019).
- [20] C. M. Bender and S. Boettcher, *Phys. Rev. Lett.* **80**, 5243 (1998).
- [21] C. E. Rüter, K. G. Makris, R. El-Ganainy, D. N. Christodoulides, M. Segev, and D. Kip, *Nat. Phys.* **6**, 192 (2010).
- [22] Y. D. Chong, L. Ge, H. Cao, and A. D. Stone, *Phys. Rev. Lett.* **105**, 053901 (2010).
- [23] S. Longhi, *Phys. Rev. A* **82**, 031801(R) (2010).
- [24] M. Liertzer, L. Ge, A. Cerjan, A. D. Stone, H. E. Türeci, and S. Rotter, *Phys. Rev. Lett.* **108**, 173901 (2012).
- [25] Y. Lumer, Y. Plotnik, M. C. Rechtsman, and M. Segev, *Phys. Rev. Lett.* **111**, 263901 (2013).
- [26] H. Hodaei, M.-A. Miri, M. Heinrich, D. N. Christodoulides, and M. Khajavikhan, *Science* **346**, 975 (2014).
- [27] M. Brandstetter, M. Liertzer, C. Deutsch, P. Klang, J. Schöberl, H. Türeci, G. Strasser, K. Unterrainer, and S. Rotter, *Nat. Commun.* **5**, 4034 (2014).
- [28] Z. J. Wong, Y.-L. Xu, J. Kim, K. O'Brien, Y. Wang, L. Feng, and X. Zhang, *Nat. Photon.* **10**, 796 (2016).
- [29] A. U. Hassan, B. Zhen, M. Soljacic, M. Khajavikhan, and D. N. Christodoulides, *Phys. Rev. Lett.* **118**, 093002 (2017).
- [30] B. Peng, S. K. Özdemir, F. Lei, F. Monifi, M. Gianfreda, G. Long, S. Fan, F. Nori, C. Bender, and L. Yang, *Nat. Phys.* **10**, 394 (2014).
- [31] L. Chang, X. Jiang, S. Hua, C. Yang, J. Wen, L. Jiang, G. Li, G. Wang, and M. Xiao, *Nat. Photon.* **8**, 524 (2014).
- [32] J. Zhang, B. Peng, S. K. Özdemir, Y.-X. Liu, H. Jing, X.-Y. Lü, Y.-L. Liu, L. Yang, and F. Nori, *Phys. Rev. B* **92**, 115407 (2015).
- [33] X. Zhou and Y. D. Chong, *Opt. Express* **24**, 6916 (2016).
- [34] S. Assaworarrat, X. Yu, and S. Fan, *Nature (London)* **546**, 387 (2017).
- [35] H. Wang, S. Assaworarrat, and S. Fan, *Opt. Lett.* **44**, 638 (2019).
- [36] A. U. Hassan, H. Hodaei, M.-A. Miri, M. Khajavikhan, and D. N. Christodoulides, *Phys. Rev. A* **92**, 063807 (2015).
- [37] A. U. Hassan, H. Hodaei, M.-A. Miri, M. Khajavikhan, and D. N. Christodoulides, *Phys. Rev. E* **93**, 042219 (2016).
- [38] P. Witonski, A. Mossakowska-Wyszynska, and P. Szczepanski, *IEEE J. Quantum Electron.* **53**, 2100111 (2017).
- [39] D. V. Novitsky, A. Karabchevsky, A. V. Lavrinenko, A. S. Shalin, and A. V. Novitsky, *Phys. Rev. B* **98**, 125102 (2018).
- [40] V. Sandoghdar, F. Treussart, J. Hare, V. Lefevre-Seguin, J.-M. Raimond, and S. Haroche, *Phys. Rev. A* **54**, R1777 (1996).
- [41] L. Yang and K. J. Vahala, *Opt. Lett.* **28**, 592 (2003).
- [42] L. Yang, D. K. Armani, and K. J. Vahala, *Appl. Phys. Lett.* **83**, 825 (2003).
- [43] B. Min, T. J. Kippenberg, L. Yang, K. J. Vahala, J. Kalkman, and A. Polman, *Phys. Rev. A* **70**, 033803 (2004).
- [44] A. Polman, B. Min, J. Kalkman, T. J. Kippenberg, and K. J. Vahala, *Appl. Phys. Lett.* **84**, 1037 (2004).
- [45] L. Yang, T. Carmon, B. Min, and S. M. Spillane, *Appl. Phys. Lett.* **86**, 091114 (2005).
- [46] J. Kalkman, A. Tchebotareva, A. Polman, T. J. Kippenberg, B. Min, and K. J. Vahala, *J. Appl. Phys.* **99**, 083103 (2006).
- [47] T. J. Kippenberg, J. Kalkman, A. Polman, and K. J. Vahala, *Phys. Rev. A* **74**, 051802(R) (2006).
- [48] L. He, Ş. K. Özdemir, J. Zhu, and L. Yang, *Opt. Lett.* **35**, 256 (2010).
- [49] H. Fan, S. Hua, X. Jiang, and M. Xiao, *Laser Phys. Lett.* **10**, 105809 (2013).
- [50] S. Zhu, L. Shi, B. Xiao, X. Zhang, and X. Fan, *ACS Photonics* **5**, 3794 (2018).
- [51] F. Lei, B. Peng, S. K. Ozdemir, G. Long, and L. Yang, *Appl. Phys. Lett.* **105**, 101112 (2014).
- [52] J. Wen, X. Jiang, M. Zhang, L. Jiang, S. Hua, H. Wu, C. Yang, and M. Xiao, *Photonics* **2**, 498 (2015).
- [53] X. F. Liu, F. Lei, M. Gao, X. Yang, C. Wang, S. K. Ozdemir, L. Yang, and G. Long, *Opt. Express* **24**, 9550 (2016).
- [54] X. Jiang, C. Yang, H. Wu, S. Hua, L. Chang, Y. Ding, Q. Hua, and M. Xiao, *Sci. Rep.* **6**, 38972 (2016).
- [55] X.-F. Liu, T.-J. Wang, and C. Wang, *Opt. Lett.* **43**, 326 (2018).
- [56] X.-F. Liu, F. Lei, T.-J. Wang, G.-L. Long, and C. Wang, *Nanophotonics* **8**, 127 (2019).
- [57] P. M. Becker, A. A. Olsson, and J. R. Simpson, *Erbium-Doped Fiber Amplifiers: Fundamentals and Technology* (Elsevier, New York, 1999).
- [58] R. S. Quimby, W. J. Miniscalco, and B. Thompson, *J. Appl. Phys.* **76**, 4472 (1994).
- [59] H. L. An, E. Y. B. Pun, H. D. Liu, and X. Z. Lin, *Opt. Lett.* **23**, 1197 (1998).
- [60] H. A. Haus, *Waves and Fields in Optoelectronics* (Prentice-Hall, Englewood Cliffs, NJ, 1984).
- [61] T. Kippenberg, S. Spillane, and K. Vahala, *Opt. Lett.* **27**, 1669 (2002).
- [62] E. Delevaque, T. Georges, M. Monerie, P. Lamouler, and J.-F. Bayon, *IEEE Photonic Technol. Lett.* **5**, 73 (1993).
- [63] F. Sanchez, P. Le Boudec, P.-L. François, and G. Stephan, *Phys. Rev. A* **48**, 2220 (1993).
- [64] J. L. Wagener, P. F. Wysocki, M. J. F. Digonnet, H. J. Shaw, and D. J. DiGiovanni, *Opt. Lett.* **18**, 2014 (1993).
- [65] E. Maurice, G. Monnom, B. Dussardier, and D. Ostrowsky, *Opt. Lett.* **20**, 2487 (1995).
- [66] T. Carmon, L. Yang, and K. J. Vahala, *Opt. Express* **12**, 4742 (2004).
- [67] Y. Zhou, Y. L. Lam, S. S. Wang, H. L. Liu, C. H. Kam, and Y. C. Chan, *Appl. Phys. Lett.* **71**, 587 (1997).
- [68] M. Fukushima, N. Managaki, M. Fujii, H. Yanagi, and S. Hayashi, *J. Appl. Phys.* **98**, 024316 (2005).
- [69] A. Biswas, G. S. Maciel, R. Kapoor, C. S. Friend, and P. N. Prasad, *Appl. Phys. Lett.* **82**, 2389 (2003).
- [70] H. Takashima, H. Fujiwara, S. Takeuchi, K. Sasaki, and M. Takahashi, *Appl. Phys. Lett.* **90**, 101103 (2007).
- [71] A. T. Rosenberger, L. A. Orozco, H. J. Kimble, and P. D. Drummond, *Phys. Rev. A* **43**, 6284 (1991).